doi:10.1038/nature09776

Supplementary Information for 'Unnaturally high refractive index terahertz metamaterial'

Muhan Choi, Seung Hoon Lee, Yushin Kim, Seung Beom Kang, Jonghwa Shin,
Min Hwan Kwak, Kwang-Young Kang, Yong-Hee Lee, Namkyoo Park & Bumki Min

Here, in this supplementary information, we present a detailed theoretical analysis and experimental data regarding the polarization dependency, the design of two-dimensionally isotropic high index metamaterials, the refractive indices at oblique incidence, the influence of metallic-patch thickness and central beam width variations on the effective magnetic permeability, the effective refractive index of multilayer metamaterials with large interlayer spacing, and the empirical asymptotic behaviours of the effective refractive index of the proposed high index metamaterials.

I. Polarization dependency of high refractive index metamaterials

The proposed metamaterials exhibit polarization dependency because of the structural anisotropy of the unit cell. In order to verify this dependency, a high-index metamaterial was characterized twice with the rotation of the sample by 90 degrees around the propagation axis of the incident terahertz wave (See insets of Fig. S1 for the direction of each polarization). The effective refractive indices were then compared for these two mutually orthogonal polarizations of the incident wave (Fig. S1).

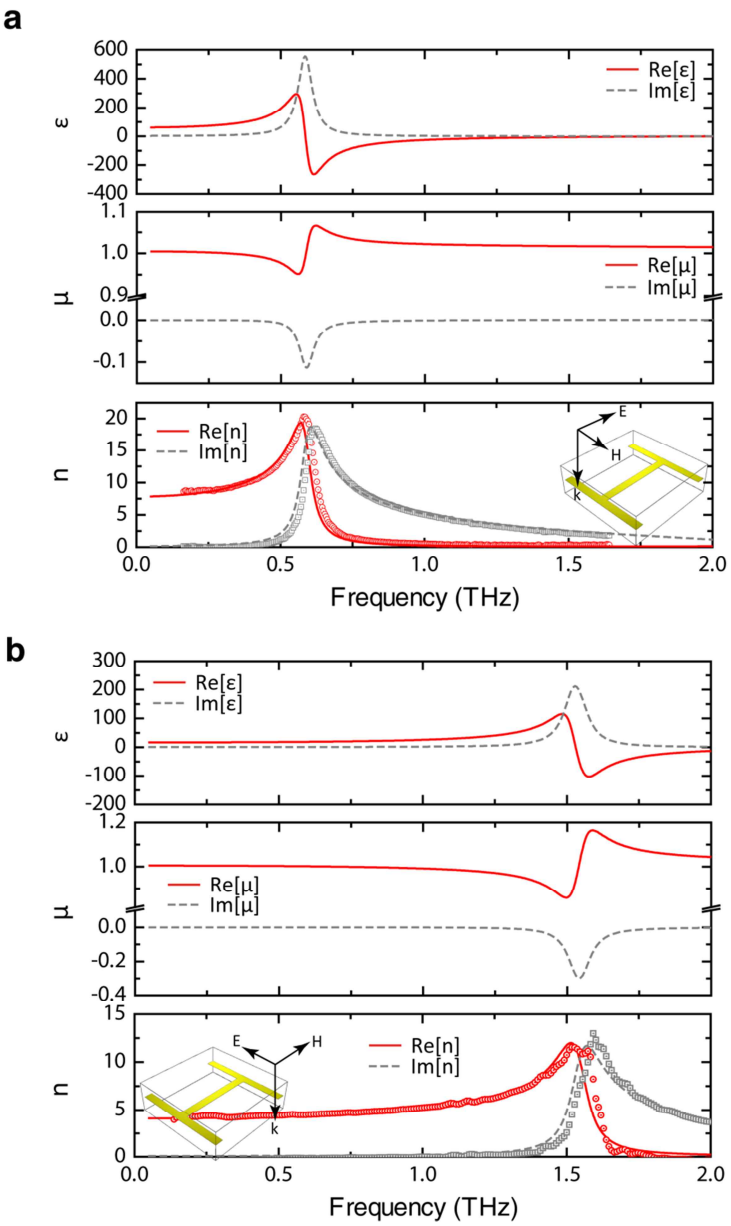

Figure S1. **Polarization dependency of a high refractive index metamaterial.** **a**, Effective permittivity (top panel) and permeability (second panel) extracted for a parallel polarization (relative to the central beam). Experimentally obtained complex refractive indices (third panel) along with the numerically extracted values from the S-parameter retrieval method (third panel). **b**, Effective parameters for the orthogonal polarization relative to the central beam. Here, the gap width g is set to 2.42 μm, the length of unit cell L is 60 μm, the width of metallic structure w is 3 μm, and the thickness d of the unit cell is 4 μm.

When the electric field of the incident wave is polarized along the central beam (defined here as a parallel polarization, Fig. S1a), higher refractive indices (both peak and quasi-static limiting values) are observed compared with the case of orthogonal polarization (in which the incident electric field is in a direction orthogonal to the central beam). This higher refractive index results from a larger capacitance of the structure for the case of parallel polarization. In addition, because of the larger capacitance, the frequency of the peak refractive index is substantially lower for the case of parallel polarization.

II. Demonstration of two-dimensionally isotropic high index metamaterials

In order to access the feasibility of isotropic high index metamaterials, we have fabricated two different types of 2D isotropic high index metamaterials and conducted additional experiments and analyses to verify the polarization independency. Figure S2a shows the polarization-angle-resolved refractive indices for a single-layer honeycomb metamaterials, of which the metamaterial is composed of an array of hexagonal metallic (gold) structure in the polyimide film ($n = 1.8 + 0.04i$). The electric field direction of incident terahertz wave is illustrated in the inset. As clearly seen from the plot (Fig. S2a), the honeycomb metamaterials exhibit polarization-insensitive refractive indices within the experimental error. As an another example, we fabricated and tested a window-type high index metamaterial (see the inset of Fig. S2b for the structural details). In addition to the 2D isotropy of refractive indices, this window-type metamaterial has advantages over I-shaped metamaterials of the same unit cell size for exhibiting higher electrical resonant frequency. Higher resonant frequency makes it possible to utilize broader high refractive index with low loss and large transmission. The polarization-angle-resolved refractive indices for the window-type high index metamaterials are shown in Fig. S2b,

which shows similar polarization independency along with higher electrical resonance frequency as predicted.

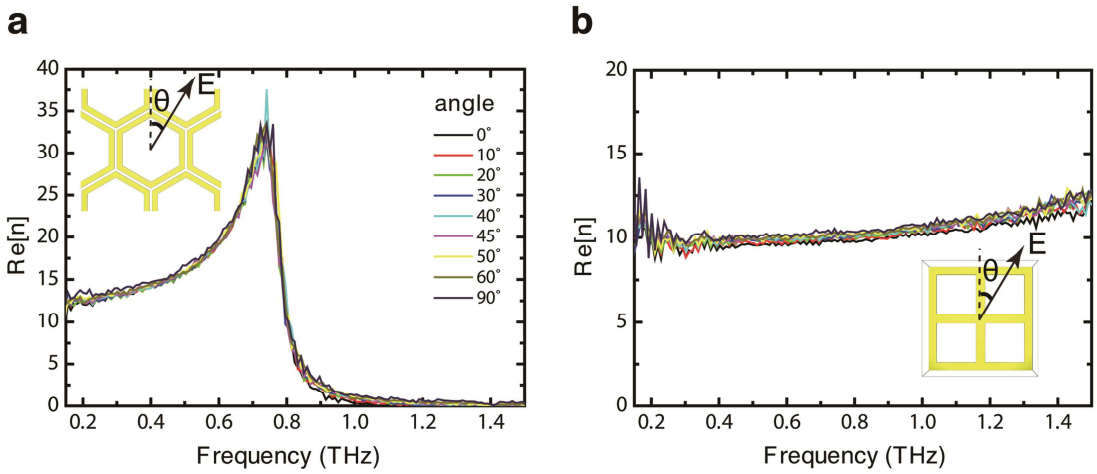

Figure S2. Two-dimensionally isotropic high index metamaterials. **a**, Polarization-angle-resolved effective refractive index for a single layer hexagonal high index metamaterial. Here, the gap width is 1.5 μm and the thickness is 1.82 μm. **b**, Polarization-angle-resolved effective refractive index for a single layer window-type high index metamaterial. Here, the gap width is 1.5 μm and the thickness is 1.82 μm.

III. Effective refractive indices at oblique incidence

To investigate the variation of effective refractive index with oblique incidence, we performed further THz-TDS measurements, in which the metamaterial samples were rotated by an encoded amount of angles with respect to the incident wave (See Fig. S3a for the geometry). Due to finite sample size (2×2 cm^2) and THz beam diameter (~0.5 cm), the maximum angle of rotation was limited to around 55° from the surface normal. For the analyses of the experimental data, the *n-k* extraction method was extended to include the effect of oblique incidence[1]. Two examples of angularly-resolved spectroscopic data are given below for your reference (each corresponding to the samples

used for Figs. 2a and 2b of the original manuscript). Interestingly, the high index metamaterials are found to be quite robust to the incidence angle (up to approximately 50°; acceptance angle of 100° around the surface normal) as can be confirmed from Fig. S3. This robustness has its origin in the weak dependency of effective permeability on the direction of incident magnetizing field (*H*).

Concerning the possibility of breakdown of the effective medium approach for oblique incidence, it is necessary to check if the effective medium condition in the transverse (*xy* plane) direction is satisfied. Being cast in more quantitative form, the in-plane projection of wavevector ($k_x = \frac{2\pi}{\lambda}\sin\theta$) should be smaller (by at least five times) than the in-plane reciprocal lattice constant ($K = \frac{2\pi}{\Lambda}$) of the high index metamaterial. This leads to the following condition: $\sin\theta \lesssim \lambda/(5\Lambda)$. Considering the maximum operating frequency of 1 THz (corresponding to the experimental data shown in Fig. S3b: $\Lambda = 60$ μm), all incident angles will be within the effective medium assumption. For the case of a multilayer metamaterial (Fig. S3c), the unit cell length in the transverse dimension is $\Lambda = 40$ μm; therefore, the condition yields a maximum angle of 48.6° (assuming the maximum operating frequency of 2 THz), within which the effective medium approach can be treated as valid. However, we think that this issue needs to be more carefully addressed in future works.

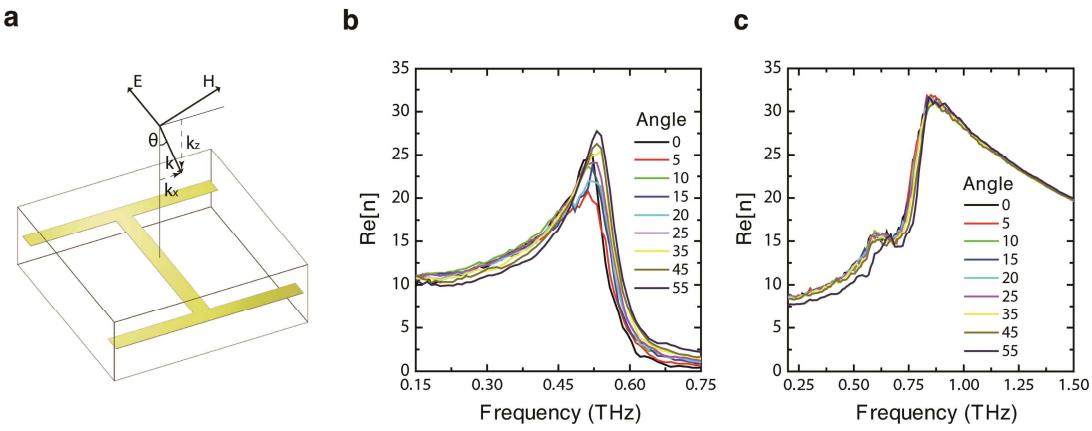

Figure S3. Effective refractive indices at oblique incidence. **a**, Schematic view on the oblique incidence. **b**, Changes in the effective refractive index with varying angle of incidence for a single layer high index metamaterial (corresponding to Fig. 2a of the original manuscript). **c**, Changes in the effective refractive index with varying angle of incidence for a five layer high index metamaterial (corresponding to Fig. 2b of the original manuscript).

IV. Influence of metallic-patch thickness/central beam width variations on the effective permeability

As briefly discussed in the main manuscript, employing a *thin* I-shaped metallic patch in the unit cell can effectively reduce a diamagnetic effect. In order to verify this geometrical shape/size dependency, the effective permeability is numerically estimated for samples having different geometrical parameters. First, the dependency of effective permeability on the central beam width (w_c) is plotted in Fig. S4a. For this simulation, the thickness of the metallic patch was fixed at 2.45 μm. In the plot, it is clearly shown that the effective permeability increases gradually and the value approaches unity over the frequency band of interest as the central beam width w_c decreases. This observation indicates that the diamagnetic effect can be effectively reduced by the use of a narrow beam in the metallic patch as a result of the decrease in the volume subtended by current

loops normal to the applied magnetizing field. It is also worthwhile to note that, in addition to reducing the diamagnetic effect, the central beam width control can be used to tune the electric resonance frequency of the metamaterial, which is caused by the change in the inductance of the metallic patch.

Another decisive factor in minimizing the diamagnetic effect is the thickness of the metallic patch. In Fig. S4b, the change of effective permeability with a variation in the thickness of the metal patch of the metamaterial is plotted. The permeability plot (Fig. S4b) shows that the decrease in metal thickness also leads to the reduction in the diamagnetic effect, which can be explained similarly to the case of width variations. Moreover, if the metal thickness is sufficiently thin enough, the diamagnetic effect is minimal, regardless of the shape of the metallic patch.

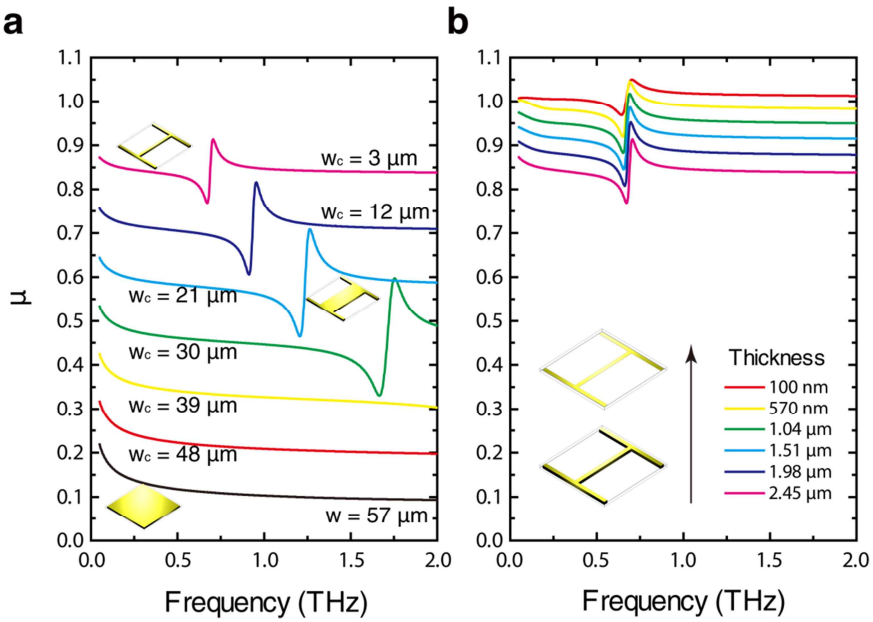

Figure S4. **Geometrical parameter-dependent effective permeability.** **a**, Effective permeability plotted as a function of central beam width. Here, the gap width g is set to 2.42 μm, the length of unit cell L is 60 μm, and the thickness d of the unit cell is 2.45 μm. The thickness of the metallic patch is also set to 2.45 μm. **b**, Effective permeability plotted as a function of metallic patch thickness.

V. Effective refractive index for multilayer metamaterials with large interlayer spacing

In this section, we provide effective refractive indices for multilayer metamaterials with large interlayer spacing (the same metamaterials for which the transmission spectra are shown in Fig. 3 of the main manuscript). The effective refractive index profiles are similar to that given in Fig. 2b (of the main manuscript) for the five-layer metamaterial except for the lower values of the indices because of the increased interlayer spacing and the decreased density of metallic layers in the metamaterial. As can be confirmed in Fig. S5, the indices of refraction converge rapidly for lower frequency ranges (up to the electrical resonant frequency) as the number of metamaterial layers increases. However, it is also noteworthy that the index of refraction converges to slightly different values (in the high frequency ranges) depending on the parity of the number of layers. This parity-dependence is attributed to the different strengths of magnetic response formed by the current loop.

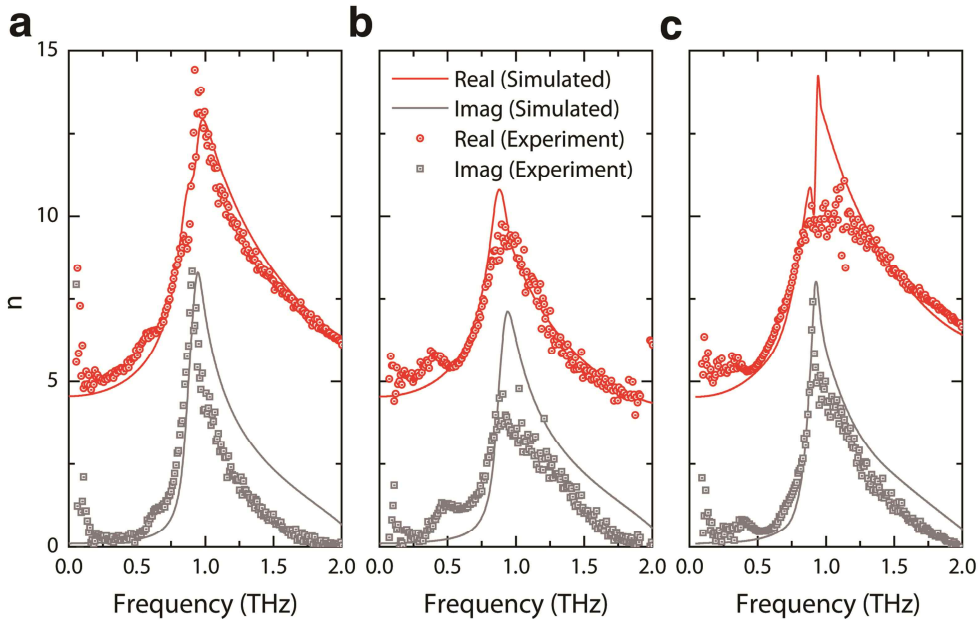

Figure S5. **Effective refractive indices for multilayer metamaterials with large interlayer spacing.** **a**, Double-layer metamaterial. **b**, triple-layer metamaterial, and **c**, four-layer metamaterial.

VI. Asymptotic behaviours of effective refractive index

The asymptotic formula for the refractive index of a single-layer metamaterial can be obtained by simplifying the geometry of the proposed metamaterials to an array of finite length line capacitors as the charges are accumulated near the edge of a thin I-shaped metallic patch upon the illumination of the terahertz wave (in the next section, we will consider the limitations of this approximation). At the static condition (corresponding to the quasi-static regime), the *total* electric field at the centre of the unit cell (or central beam) should be zero in order not to induce a current flow in the central beam. By summing electric field contributions from all the line charges, we obtain

$$E_y\big|_{centre} = \frac{\sigma}{2\pi\varepsilon_0\varepsilon_p}\left\{\sum_{n=0}^{\infty}\int_{-(L-g)/2}^{(L-g)/2}\frac{\left(\frac{L-g}{2}+nL\right)(-dx)}{\left[x^2+\left(\frac{L-g}{2}+nL\right)^2\right]^{3/2}}\right.$$

$$+2\sum_{m=1}^{\infty}\sum_{n=0}^{\infty}\int_{-(L-g)/2}^{(L-g)/2}\frac{\left(\frac{L-g}{2}+nL\right)(-dx)}{\left[(x+mL)^2+\left(\frac{L-g}{2}+nL\right)^2\right]^{3/2}}$$

$$+\sum_{n=0}^{\infty}\int_{-(L-g)/2}^{(L-g)/2}\frac{\left(\frac{L+g}{2}+nL\right)dx}{\left[x^2+\left(\frac{L+g}{2}+nL\right)^2\right]^{3/2}}$$

$$\left.+2\sum_{m=1}^{\infty}\sum_{n=0}^{\infty}\int_{-(L-g)/2}^{(L-g)/2}\frac{\left(\frac{L+g}{2}+nL\right)dx}{\left[(x+mL)^2+\left(\frac{L+g}{2}+nL\right)^2\right]^{3/2}}\right\},$$

where ε_p is the relative permittivity of the substrate material and σ is the line charge density. For simplicity, four integrations in the above equation can be analytically carried out and are denoted below as A, B, C and D. Then, the expression for the electric field can be cast in a simpler form,

$$E_y\big|_{centre} = \frac{\sigma}{2\pi\varepsilon_0\varepsilon_p}\left\{\sum_{n=0}^{\infty}A(g,L;n)+2\sum_{m=1}^{\infty}\sum_{n=0}^{\infty}B(g,L;n,m)+\sum_{n=0}^{\infty}C(g,L;n)\right.$$

$$\left.+2\sum_{m=1}^{\infty}\sum_{n=0}^{\infty}D(g,L;n,m)\right\},$$

where A, B, C, and D are explicitly written as follow,

$$A(g,L;n) = \frac{2\sqrt{2}(L-g)}{\{g-L(2n+1)\}\sqrt{g^2-2gL(n+1)+L^2\{1+2n(n+1)\}}},$$

$$B(g,L;n,m)$$

$$= -\frac{\sqrt{2}\{g+L(2m-1)\}}{\{g-L(2n+1)\}\sqrt{g^2+2gL(m-n-1)+L^2(1-2m+2m^2+2n+2n^2)}}$$

$$+\frac{\sqrt{2}\{-g+L(2m+1)\}}{\{g-L(2n+1)\}\sqrt{g^2-2gL(m+n+1)+L^2(1+2m+2m^2+2n+2n^2)}},$$

$$C(g,L;n) = \frac{2\sqrt{2}(L-g)}{\{g+L(2n+1)\}\sqrt{g^2-2gLn+L^2\{1+2n(n+1)\}}},$$

$$D(g,L;n,m)$$

$$= -\frac{\sqrt{2}\{g+L(2m-1)\}}{\{g+L(2n+1)\}\sqrt{g^2+2gL(m+n)+L^2(1-2m+2m^2+2n+2n^2)}}$$

$$+\frac{\sqrt{2}\{-g+L(2m+1)\}}{\{g+L(2n+1)\}\sqrt{g^2+2gL(-m+n)+L^2(1+2m+2m^2+2n+2n^2)}}.$$

Under the quasi-static limit, the *total* electric field should be zero.

$$0 = E_y\big|_{centre} + E_{in},$$

where E_{in} is the applied electric field. Using the above equations, the amount of accumulated charges can be estimated as a function of the geometrical parameters (g and L) and the applied electric field (E_{in}).

$$Q = \sigma(L-g) = -\frac{2\pi\varepsilon_0\varepsilon_p(L-g)E_{in}}{\sum_{n=0}^{\infty}A + 2\sum_{m=1}^{\infty}\sum_{n=0}^{\infty}B + \sum_{n=0}^{\infty}C + 2\sum_{m=1}^{\infty}\sum_{n=0}^{\infty}D}.$$

In a neighbourhood of $g = 0$ (strongly-coupled regime), the formula for accumulated charges can be expanded in a Taylor series and found to be proportional to $L^3 g^{-1}$ to the first order,

$$Q \propto \varepsilon_0\varepsilon_p \frac{L^3}{g} E_{in}.$$

While in a neighbourhood of $g = L$ (weakly-coupled regime),

$$Q \propto \varepsilon_0 \varepsilon_p (L-g)^2 E_{\hat{\boldsymbol{n}}} .$$

As described in the main manuscript, the scaling behaviour of accumulated charges is substantially different for each of the regimes. Once the amount of charges accumulated on each arm of the line capacitor is estimated, the effective (relative) permittivity of the metamaterial can be obtained using the following relationship (where χ_m is the effective susceptibility contribution from the metallic patch),

$$\varepsilon_r \simeq 1 + \chi_p + \chi_m = \varepsilon_p + \frac{P}{\varepsilon_0 E}.$$

Here, the polarization density can be approximated as the dipole moment per unit volume,

$$P = \frac{Q(L-g)}{L^2 d}.$$

Note that we have used the physical thickness instead of effective thickness for simplicity. By introducing the following *empirical* relation,

$$E = \left(\frac{L}{g}\right)^{\beta} E_{\hat{\boldsymbol{n}}} .$$

where β is a dimensionless fitting parameter, the effective refractive index of a single-layer metamaterial can be approximated as (with the assumption of effective permeability being unity),

$$n \simeq \sqrt{\varepsilon_p + \frac{P}{\varepsilon_0 E}}$$

$$= n_p \sqrt{1 - \frac{2\pi\alpha}{d}\left(1-\frac{g}{L}\right)^2 \left(\frac{g}{L}\right)^{\beta} \left(\sum_{n=0}^{\infty} A + 2\sum_{m=1}^{\infty}\sum_{n=0}^{\infty} B + \sum_{n=0}^{\infty} C + 2\sum_{m=1}^{\infty}\sum_{n=0}^{\infty} D\right)^{-1}} .$$

where α is another dimensionless fitting parameter that corrects the deviation observed in actual samples from an ideal situation (such as loss of the substrate, finite width, and thickness of the metallic structure and charge distribution in the I-shaped metallic patch, etc). By expanding this in a neighbourhood of $g = 0$ and L (Taylor series expansion), we finally obtain the empirical asymptotic formula for the effective refractive index as given in the main manuscript,

$$n \simeq n_p \left\{1 + \frac{\pi\alpha L}{2\sqrt{2}d}\left(1 - \frac{g}{L}\right)^3 + \frac{\pi\alpha\beta L}{2\sqrt{2}d}\left(1 - \frac{g}{L}\right)^4\right\} \quad (g \lesssim L)$$

$$n \propto n_p \alpha^{1/2} d^{-1/2} L^{(2-\beta)/2} g^{-(1-\beta)/2} \quad (g \ll L)$$

In addition to the comparison (Fig. 4a) given in the main manuscript, we provide more examples of fitting results for various samples in Fig. S6. Here, all the plots are generated for samples having a metallic patch width of 200 nm and a thickness of 100 nm. The fitting parameter α ranges from 0.284 to 0.571 and the parameter β stays near the value between 0.541 and 0.672 for the simulated cases (Fig. S6).

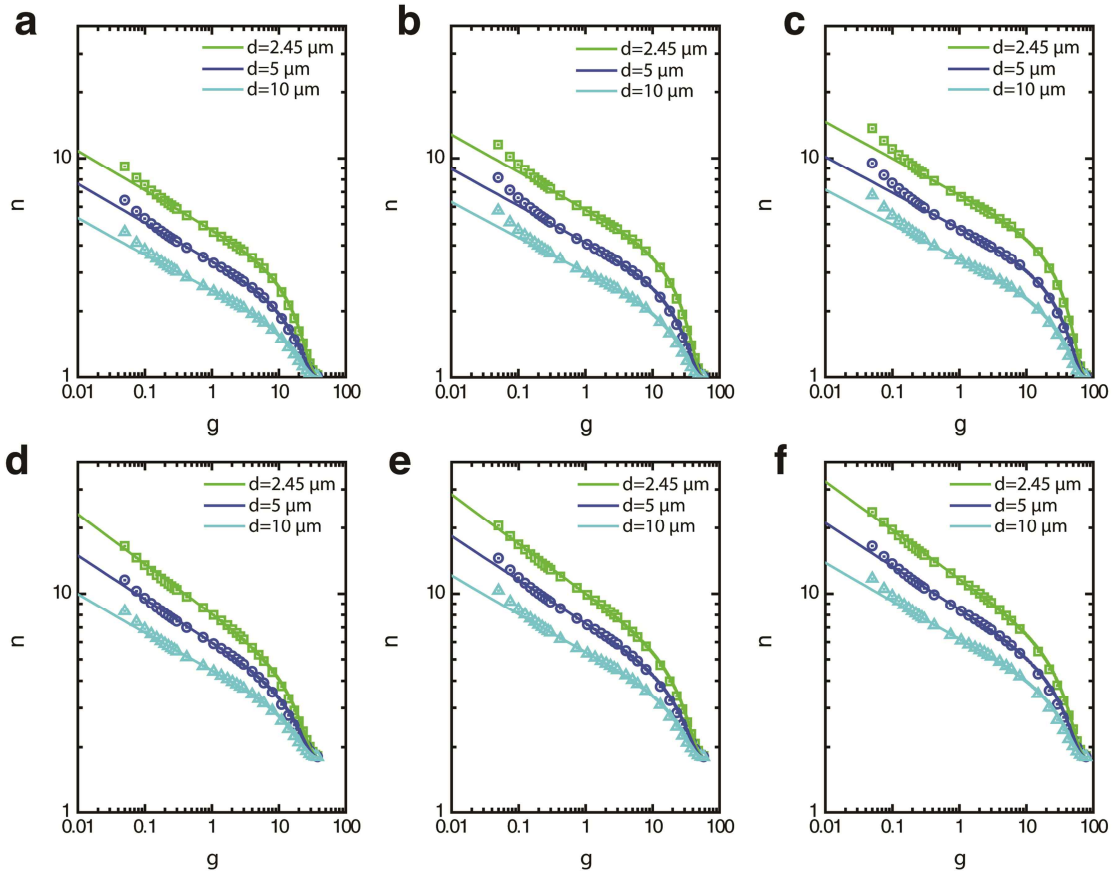

Figure S6. **Effective refractive index as a function of the gap width near the quasi-static limit (f = 0.05 THz).** Simulated values are plotted with the scatters and the asymptotic fittings are drawn with lines. **a**, $n_p = 1$, $L = 40$ μm. **b**, $n_p = 1$, $L = 60$ μm. **c**, $n_p = 1$, $L = 80$ μm. **d**, $n_p = 1.8$, $L = 40$ μm. **e**, $n_p = 1.8$, $L = 60$ μm. **f**, $n_p = 1.8$, $L = 80$ μm.

VII. Comment on the limitation of the line charge assumption

The influence of the finite thickness and width of the metallic patch was neglected in the assumption made previously in the derivation of the asymptotic formula for the effective refractive index and the errors made in the course of derivation are lumped into two fitting parameters. However, as the gap width becomes comparable to the thickness of the metallic patch, a parallel plate model becomes more accurate than the parallel line

model. The formula for the capacitance of a parallel plate capacitor including the effect of a fringing field was slightly modified to be applied to our proposed geometry[2],

$$C \simeq \varepsilon_0 \varepsilon_p \left\{ 1.15 \left(\frac{2t}{g} \right) + 2.80 \left(\frac{2w}{g} \right)^{0.22} \right\} (L - g)$$

As the effective permittivity is proportional to the capacitance, the refractive index is supposed to be proportional to $\sqrt{C}$ with the assumption of effective permeability being unity.

$$n \propto \sqrt{C} \simeq n_p \sqrt{\varepsilon_0 \left\{ 1.15 \left(\frac{2t}{g} \right) + 2.80 \left(\frac{2w}{g} \right)^{0.22} \right\} (L - g)}$$

The capacitance is composed of two contributions each having different asymptotic behaviours in the limit of $g \to 0$. The first term dominates over the second term and the refractive index will increase with a rate $g^{-1/2}$.

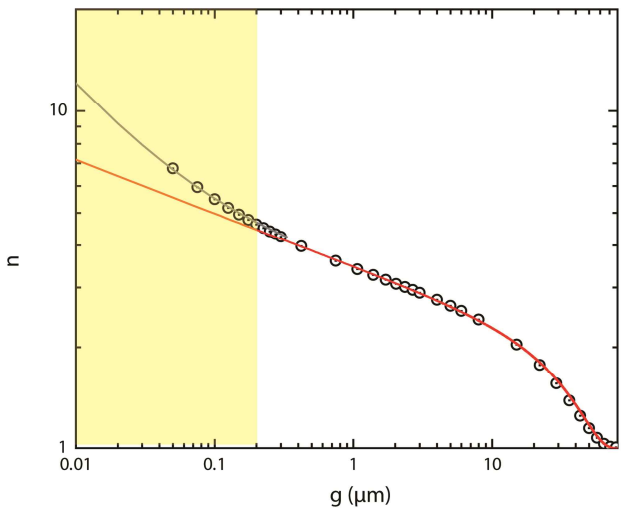

Figure S7. Simulated refractive index (scatters), asymptotic (red line), and parallel plate capacitor approximation (gray line).

VIII. Field plot for a single layer metamaterial at various frequencies

Here, we present magnetic field plots for a single-layer metamaterial (See Fig. 1c, d in the main manuscript) at three different frequencies. Close to a quasi-static regime (at $f = 0.1$ THz), the magnetic field penetrates deeply into the unit cell (Fig. S8a). As the frequency approaches that of electric resonance ($f = 0.66$ THz, in this specific example, Fig. S8c), the magnetic field still penetrates deeply into the unit cell while the strongest magnetic field contributions result from the current flowing in the central beam.

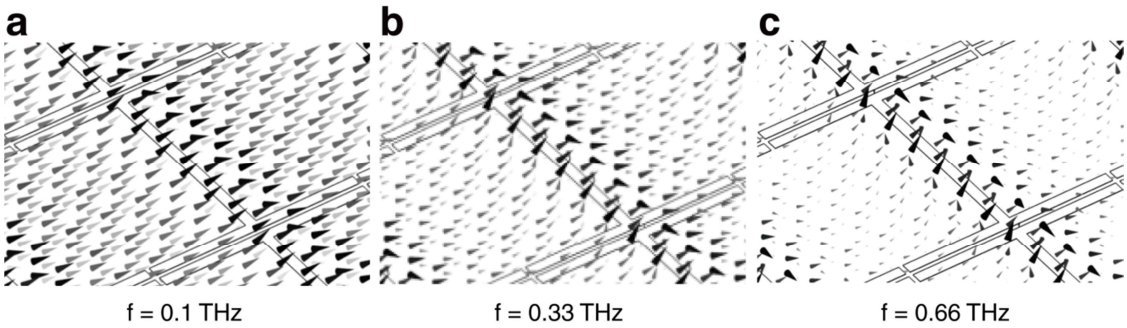

Figure S8. Magnetic field plot for three different frequencies in a single-layer metamaterial.

References

1. Dorney, D. T., Baraniuk, G. R. & Mittleman, M. D. Material parameter estimation with terahertz time-domain spectroscopy. *J. Opt. Soc. Am. A* **18,** 1562-1571 (2001).

2. Sakurai, T. & Tamaru, K. Simple formulas for two- and three-dimensional capacitances. *IEEE Trans. Electron Devices* **ED-30,** 183-185 (1983).